European Radiology (2022) 32:8659–8669
https://doi.org/10.1007/s00330-022-08911-3

MAGNETIC RESONANCE

MRI-based radiomics signature for identification of invisible basal cisterns changes in tuberculous meningitis: a preliminary multicenter study

Qiong Ma[1,2] · Yinqiao Yi[3] · Tiejun Liu[4] · Xinnian Wen[5] · Fei Shan[1] · Feng Feng[6] · Qinqin Yan[1] · Jie Shen[1] · Guang Yang[3] · Yuxin Shi[1]

Received: 4 December 2021 / Revised: 27 April 2022 / Accepted: 27 May 2022 / Published online: 24 June 2022

Abstract

Objective To develop and evaluate a radiomics signature based on magnetic resonance imaging (MRI) from multicenter datasets for identification of invisible basal cisterns changes in tuberculous meningitis (TBM) patients.

Methods Our retrospective study enrolled 184 TBM patients and 187 non-TBM controls from 3 Chinese hospitals (training dataset, 158 TBM patients and 159 non-TBM controls; testing dataset, 26 TBM patients and 28 non-TBM controls). nnU-Net was used to segment basal cisterns in fluid-attenuated inversion recovery (FLAIR) images. Subsequently, radiomics features were extracted from segmented basal cisterns in FLAIR and T2-weighted (T2W) images. Feature selection was carried out in three steps. Support vector machine (SVM) and logistic regression (LR) classifiers were applied to construct the radiomics signature to directly identify basal cisterns changes in TBM patients. Finally, the diagnostic performance was evaluated by the receiver operating characteristic (ROC) curve analysis, calibration curve, and decision curve analysis (DCA).

Results The segmentation model achieved the mean Dice coefficients of 0.920 and 0.727 in the training and testing datasets, respectively. The SVM model with 7 T2WI–based radiomics features achieved best discrimination capability for basal cisterns changes with an AUC of 0.796 (95% CI, 0.744–0.847) in the training dataset, and an AUC of 0.751 (95% CI, 0.617–0.886) with good calibration in the testing dataset. DCA confirmed its clinical usefulness.

Conclusion The T2WI–based radiomics signature combined with deep learning segmentation could provide a fully automatic, non-invasive tool to identify invisible changes of basal cisterns, which has the potential to assist in the diagnosis of TBM.

Key Points

- *The T2WI–based radiomics signature was useful for identifying invisible basal cistern changes in TBM.*
- *The nnU-Net model achieved acceptable results for the auto-segmentation of basal cisterns.*
- *Combining radiomics and deep learning segmentation provided an automatic, non-invasive approach to assist in the diagnosis of TBM.*

Keywords Magnetic resonance imaging · Tuberculous meningitis · Deep learning · Radiomics

Qiong Ma and Yinqiao Yi contributed equally to this work.

✉ Guang Yang
gyang@phy.ecnu.edu.cn

✉ Yuxin Shi
shiyuxin@shphc.org.cn

[1] Department of Radiology, Shanghai Public Health Clinical Center, Fudan University, Shanghai, China

[2] Shanghai Institute of Medical Imaging, Fudan University, Shanghai, China

[3] Shanghai Key Laboratory of Magnetic Resonance, East China Normal University, Shanghai, China

[4] Department of Radiology, Liuzhou People's Hospital, Liuzhou, Guangxi Zhuang Autonomous Region, China

[5] Department of Radiology, Guangxi Zhuang Autonomous Region Chest Hospital, Liuzhou, Guangxi Zhuang Autonomous Region, China

[6] Department of Radiology, Nantong Tumor Hospital, Nantong, Jiangsu, China

Abbreviations

AUC	Area under the curve
CSF	Cerebrospinal fluid
DCA	Decision curve analysis
DWI	Diffusion-weighted imaging
FLAIR	Fluid-attenuated inversion recovery
GLCM	Gray-level co-occurrence matrix
GLDM	Gray-level dependence matrix
GLRLM	Gray-level run length matrix
GLSZM	Gray-level size zone matrix
LoG	Laplacian of Gaussian
LR	Logistic regression
MRI	Magnetic resonance imaging
NGTDM	Neighboring gray tone difference matrix
PCC	Pearson correction coefficient
RFE	Recursive feature elimination
ROC	Receiver operating characteristic
ROI	Region of interest
SVM	Support vector machine
T2W	T2-weighted
TB	Tuberculosis
TBM	Tuberculous meningitis

Introduction

Tuberculosis (TB) is still one of the top ten causes of death globally, and before the coronavirus (COVID-19) pandemic, it was the leading cause of death from a single infectious agent [1]. Tuberculous meningitis (TBM) is the most serious form of TB, accounting for about 5–10% of extrapulmonary TB [2]. In the early stage, non-specific prodromal symptoms are typically of insidious onset, and then slowly progress to meningitis, causing enormous difficulty in the early diagnosis and subsequently the treatment of the disease [3]. Even after receiving anti-TB drug treatment, the mortality rate of TBM is still as high as 10.0–36.5% [4]. The clinical outcome mainly depends on the initial stage of treatment. Therefore, early diagnosis and treatment are of great significance for improving the prognosis of TBM patients.

Magnetic resonance imaging (MRI) is the most useful and widely available imaging method for the diagnosis and management of TBM and the affiliated complications [5]. Basal meningeal enhancement is the most consistent neuroradiological findings in TBM [6]. It shows a distinctive tendency to involve the basal cisterns in TBM, especially the suprasellar, prepontine, crural, and ambient cisterns [7]. However, the imaging finding can hardly be detected by conventional radiological examinations before advanced stages [8]. In a previous study, basal cisterns were used as region of interest (ROI) to quantitatively measure the destruction of blood-brain barriers in TBM through dynamic contrast-enhanced MR perfusion. However, in cases with low levels of blood-brain barrier disruption and minor inflammatory changes that occur in early stages, the role of dynamic contrast-enhanced MR perfusion was limited [9]. Therefore, it is still difficult to detect intracranial lesions timely, especially the invisible pathological changes of basal cisterns, which are closely associated with poor outcomes.

As a quantitative analysis approach, radiomics can convert image data of ROI into high-resolution, discoverable feature space data using automated data characterization algorithms, and finally achieves deeper analysis and application of information [10]. It has been widely used in oncologic imaging, including differential diagnosis, tumor staging, genotyping, treatment response, and patient survival prediction [11–13]. It is worth mentioning that due to the qualitative and quantitative problems in the conventional imaging diagnosis of non-neoplastic lesions, radiomics researches of non-neoplastic diseases also have important clinical value. For instance, Kassner et al demonstrated that texture analysis may identify acute ischemic stroke patients who are most likely to undergo hemorrhagic transformation with a greater accuracy than visual inspection of gadolinium enhancement [14]. Using the venous sinuses and basal cisterns as ROIs, Arnold et al achieved a high diagnostic accuracy in separating spontaneous intracranial hypotension patients and healthy controls with a fully automatic algorithm. And least axis length and volume were the best discriminating radiomics features in the suprasellar cistern [15].

To extract features from images, ROIs should be delineated first. Convolutional neural networks have been extensively applied in the medical image segmentation [16, 17]. nnU-Net is a newly proposed model for medical segmentation tasks [18], and its core design idea is to obtain more reliable segmentation results for various datasets through adaptive preprocessing and model training strategies, rather than manual parameter tuning [18, 19]. Owing to its unique advantages, it has been broadly utilized in medical image segmentation, such as coronavirus disease 2019 segmentation [20], kidney and kidney tumor segmentation [21], and breast and fibroglandular tissue segmentation [22]. Until now, no relevant research has been conducted to apply nnU-Net for the segmentation of basal cisterns.

Therefore, the present study first aimed to assess the application of nnU-Net for automatic segmentation of basal cisterns. Then, radiomics features were extracted from nnU-Net segmented ROIs and a radiomics signature was constructed to explore changes of basal cisterns in TBM patients, which might be undetectable by the naked eye on conventional MR images.

Materials and methods

Patients and MR acquisition

The retrospective study was approved by the institutional review board in all participating centers, and the requirement for written informed consent was waived. Patients with TBM were

enrolled from 3 Chinese hospitals, which consisted of the Shanghai Public Health Clinical Center (SPHCC; Shanghai, China), Guangxi Zhuang Autonomous Region Chest Hospital (GZAR-CH; Liuzhou, China), and Liuzhou People's Hospital (LPH; Liuzhou, China) from January 2015 to December 2020. The inclusion criteria were as follows: (1) patients who were diagnosed with definite or probable TBM according to Marais et al's criteria [5] and (2) patients with no definite lesions in conventional cranial MR images on admission. The exclusion criteria were as follows: (1) patients who were co-infected with other pathogens in the central nervous system; (2) patients with poor-quality MR images; and (3) patients who underwent cranial surgery or chemo-radiotherapy. The control group consisted of patients admitted in the same period with normal cranial MRI and no final clinical diagnosis involving TB infection. A total of 184 TBM patients and 187 age- and gender-matched non-TBM controls were included. The dataset was divided into training dataset (n = 317 [SPHCC (61 TBM patients + 69 non-TBM controls); GZAR-CH (97 TBM patients + 90 non-TBM controls)]) and testing dataset (n = 54 [LPH (26 TBM patients + 28 non-TBM controls]). The study flowchart is shown in Fig. 1.

All patients received conventional cranial MRI via different 1.5-T scanners. We only retrieved T2-weighted (T2W)

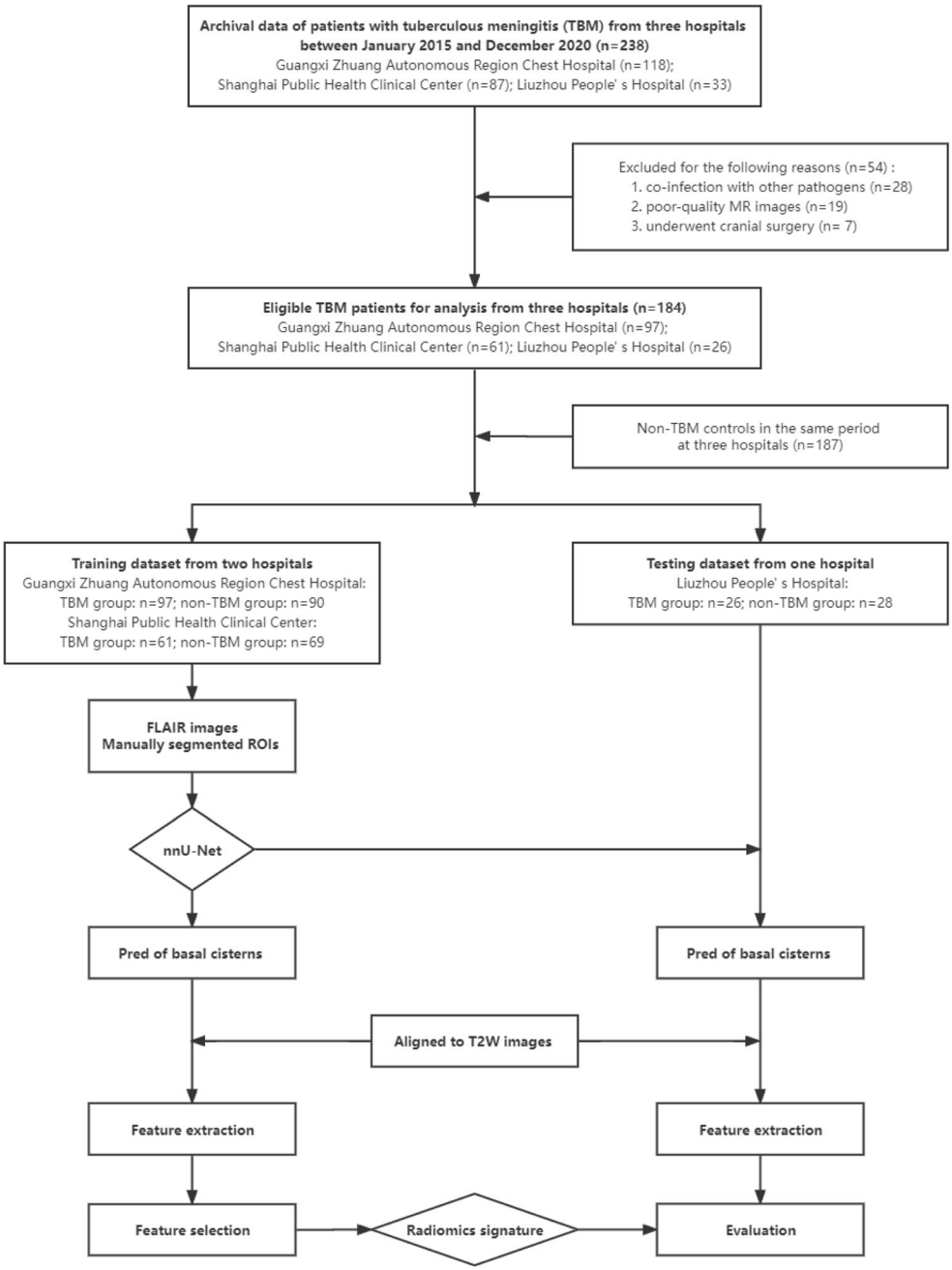

Fig. 1 Flowchart of our study

Table 1 Cranial MRI protocols of different scanners in three hospitals

Hospital	MRI model	Sequence	TR/TE (ms)	FOV (mm)	Matrix (mm)	Slice thickness (mm)
GZAR-CH	Siemens Avanto 1.5 T	T2W	4000/89	240	384*241	5
		FLAIR	6000/92	240	384*224	5
SPHCC	Philips Achieva 1.5 T	T2W	4000/110	240	256*256	5
		FLAIR	6000/120	240	256*256	5
LPH	GE HDe 1.5 T	T2W	3000/105	240	320*224	6
		FLAIR	8400/145	240	320*192	6

FLAIR fluid attenuated inversion recovery, *FOV* field of view, *GZAR-CH* Guangxi Zhuang Autonomous Region Chest Hospital, *LPH* Liuzhou People's Hospital, *SPHCC* Shanghai Public Health Clinical Center, *TE* echo time, *TR* repetition time, *T2W* T2-weighted

and FLAIR images from the picture archiving and communication system. The detailed parameters of three scanners and the MRI protocols are summarized in Table 1.

Basal cisterns segmentation

The basal cisterns were defined as ROI, including the suprasellar cistern, crural cisterns, ambient cisterns, quadrigeminal corpus cisterns, prepontine cisterns, and sylvian cisterns (Fig. 2). Manual segmentation was performed by a radiologist with 2 years of experience in neuroradiology, and the results were confirmed by another radiologist with 28 years of experience in neuroradiology using an open-source ITK-SNAP software version 3.6.0 (www.itksnap.org). The ROIs were delineated on each slice of the FLAIR images containing basal cisterns, using the corresponding T2W images as visual guidance.

To implement a fully automatic radiomics pipeline, nnU-Net was used to train a segmentation model. We utilized the two-dimensional nnU-Net [18], which is based on U-Net architecture [23], and provided as part of nnU-Net for the automated design of medical segmentation models. The input image size was set to 320 × 320 with a batch size of 32. A total of 6 down-sampling operations were performed. Leaky rectified linear unit was used as activation function, and instance normalization was employed for feature map normalization. The loss function was the sum of Dice loss and cross-entropy loss. Stochastic gradient descent with an initial learning rate of 0.01 was used for training. Five-fold cross-validation was utilized to avoid overfitting. T2W images were resampled with FLAIR images as a reference, and the resample method was sitkBSpline. Finally, automatically segmented ROIs were employed to extract radiomics features.

Feature extraction

Radiomics features were extracted from segmented ROIs in FLAIR images and T2W images which aligned to FLAIR images (normalized to the range of [0, 100]). The pixel-voxel resampling method was sitkBSpline. For Laplacian of Gaussian (LoG) filters, $\lambda = 5.0$ was used. For texture feature extraction, a fixed bin width 5 was used. In our study, the

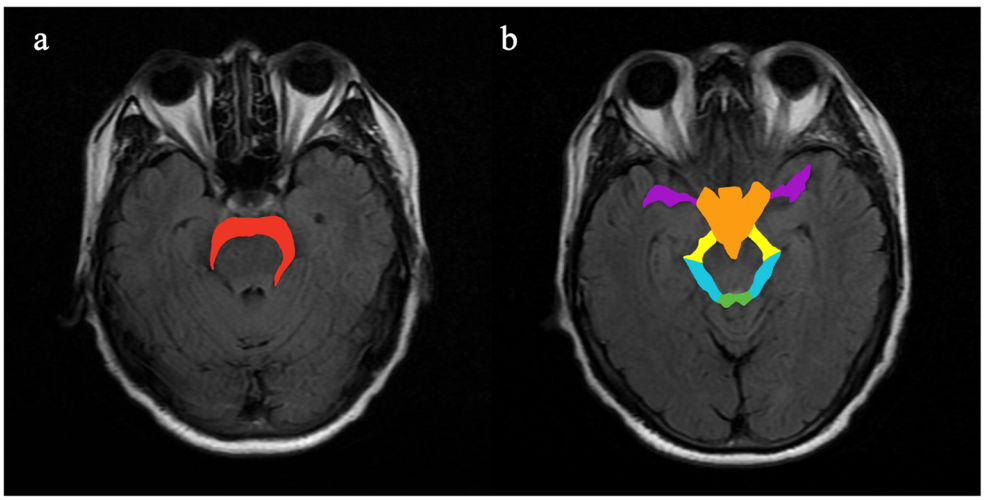

Fig. 2 Placement of the basal cisterns as ROIs on axial FLAIR images. Red color denotes the prepontine cistern (**a**). Orange, yellow, blue, green, and purple colors denote the suprasellar cistern, crural cisterns, ambient cisterns, quadrigeminal cistern, and sylvian cisterns, respectively (**b**). ROI, region of interest; FLAIR, fluid-attenuated inversion recovery

following features were extracted: (1) shape-based features; (2) first-order features; (3) texture features: gray-level co-occurrence matrix (GLCM), gray-level dependence matrix (GLDM), gray-level run length matrix (GLRLM), gray-level size zone matrix (GLSZM), and neighboring gray tone difference matrix (NGTDM). We used the up-sampling to balance positive and negative samples in the training dataset. All features were normalized to the range of [−0.5, 0.5] before further use.

Feature selection and radiomics signature development

To reduce overfitting or bias in the radiomics features, three steps were considered for feature selection. Firstly, the independent-sample *t* test was used for preliminary feature screening, and the features without significant difference between the TBM and non-TBM groups in the training dataset were removed. Secondly, the Pearson correction coefficient (PCC) analysis was employed to eliminate redundancy and to maintain independency among the features. One of the features with a high correlation (PCC > 0.90) was removed. The final step for feature selection was bound with the model building, as described below.

Support vector machine (SVM) and logistic regression (LR) were used to construct the radiomics signature, and their combinations with two feature selection algorithms, namely recursive feature elimination (RFE) and relief, were explored. For each combination, we built the model using five-fold cross-validation on the training dataset. To determine the number of features retained in the final model, the number of features was iterated from 1 to 30 using either RFE or relief, and the averaged cross-validation AUC values were plotted against the number of features. Then, the 1-SE rule was used to find the best number of features in the model; that is, the model with the smallest number of features and a cross-validation AUC within one standard error from the highest AUC was chosen as the best model.

The above-mentioned processes were undertaken using an open-source free software, Feature Explorer version 0.5.0 [24], which used PyRadiomics version 3.0 [25] and scikit-learn version 0.22.2 in the back for feature extraction and subsequent signature developing.

Validation of the radiomics signature

To evaluate the discrimination competence of the radiomics signatures, the receiver operating characteristic (ROC) curve was plotted to obtain the values of AUC in the training and testing datasets. The specificity, sensitivity, and accuracy were also calculated using a threshold value maximizing Youden index on the training and testing datasets. DeLong's test was used to compare different AUCs of radiomics signatures. Subsequently, the calibration curve was plotted to evaluate the calibration ability. Decision curve analysis (DCA) was employed to estimate the clinical usefulness of the radiomics signatures.

Statistical analysis

The statistical analyses were performed with the SPSS 22.0 software, R software version 3.6.3, and SciPy version 1.7.0 or scikit-learn version 0.24.2 on Python version 3.7.1. Features were compared by the independent-sample *t* test or the Mann-Whitney *U* test. In statistical tests of characteristics of patients, the Mann-Whitney *U* test was used for numerical variables, and the chi-square test or fisher's exact test was used for categorical variables. $p < 0.05$ indicated a statistical significance.

Results

Patient characteristics

In this study, there were 184 patients in the TBM group (male (129) vs. female (55); mean age, 39.57 ± 16.26 years old) and 187 individuals in the non-TBM group (male (121) vs. female (66); mean age, 39.75 ± 13.97 years old). The clinical characteristics of the patients are given in Table 2.

nnU-Net-based segmentation performance

The mean Dice coefficient and the 95-percentile of the average symmetric Hausdorff distance were used to evaluate the segmentation model. The mean Dice coefficient was 0.920 in the training dataset and 0.727 in the testing dataset. The Hausdorff distance values of the segmentation were 0.216 and 1.449 in the training and testing datasets, respectively. The results of manual and automatic segmentation are shown in Fig. 3.

Radiomics feature selection and radiomics signature developing

A total of 200 features were extracted from the automatically segmented basal cisterns in T2W and FLAIR images, respectively. We initially used the independent-sample *t* test to remove features whose distributions in the TBM and non-TBM groups exhibited no significant difference. The remaining features were used in further signature developing, where PCC analysis was employed for dimensionality reduction and RFE or relief for feature selection. In total, 7 T2W features were retained in the SVM model (linear kernel with C-parameter = 1.0), and 13 FLAIR features were retained in the LR model (Table 3).

Table 2 Characteristics of patients in the training and testing datasets

	Training dataset = 317			Testing dataset = 54		
	TBM (*n* = 158)	Non-TBM (*n* = 159)	*p value*	TBM (*n* = 26)	Non-TBM (*n* = 28)	*p value*
Age, y			0.526[a]			0.993[a]
Mean	39.29	39.47		41.42	41.39	
Range	18.00–79.00	18.00–81.00		18.00–77.00	24.00–72.00	
Sex (*n*, %)			0.210[b]			0.586[c]
Male	108 (68.35%)	98 (61.64%)		21 (80.77%)	23 (82.14%)	
Female	50 (31.65%)	61 (38.36%)		5 (19.23%)	5 (17.86%)	
Symptoms (*n*, %)						
Fever	121 (76.58%)			17 (65.38%)		
Headache	93 (58.86%)			13 (50.00%)		
Dizziness	16 (10.13%)			1 (3.85%)		
Vomiting	24 (15.19%)			1 (3.85%)		
Cough	19 (12.03%)			2 (7.69%)		
Convulsion	8 (5.06%)			3 (11.54%)		
Visual disorders	4 (2.53%)			0 (0.00%)		
Hearing disorder	1 (0.63%)			0 (0.00%)		
Consciousness disorders	18 (11.39%)			4 (15.38%)		
CSF tests (mean ± SD)						
White blood cell counts (*n*/μL)	143.08 ± 245.32			169.19 ± 214.48		
Protein (mg/L)	1259.41 ± 1356.07			1531.56 ± 1568.74		
Chloride (mmol/L)	115.93 ± 7.58			115.01 ± 8.70		
Glucose (mmol/L)	2.74 ± 1.61			2.20 ± 0.75		
TBM category (*n*, %)						
Definite	44 (27.85%)			9 (34.62%)		
Probable	114 (72.15%)			17 (65.38%)		

not measured, *CSF* cerebrospinal fluid, *SD* standard deviation, *TBM* tuberculous meningitis

[a] Mann-Whitney *U* test

[b] Chi-square test

[c] Fisher's exact test

Performance and validation of the radiomics signature

The results of the two radiomics signatures are shown in Fig. 4 and Table 4. Using 7 selected optimal features, the T2WI–based radiomics signature derived from the SVM classifier achieved an AUC of 0.796 (95% CI, 0.744–0.847) in the training dataset, and was then confirmed in the testing dataset with an AUC of 0.751 (95% CI, 0.617–0.886), the result of which showed a better performance compared with that of the FLAIR–based radiomics signature in the testing dataset (AUC = 0.676; 95% CI, 0.529–0.823). However, DeLong's test showed no significant difference between the above two radiomics signatures (p = 0.152).

In the training datasets, the calibration curves of the two radiomics signatures demonstrated good agreement between prediction and observation (Fig. 5a, c). In the testing datasets, the calibration curve of the T2WI–based radiomics signature exhibited better consistency than that of the FLAIR–based radiomics signature, with a mean absolute error of 0.033 and 0.047, respectively (Fig. 5b, d). The DCA is depicted in Fig. 6. The curve analysis showed that T2WI–based and FLAIR–based radiomics signature offered certain high overall net benefits, while the performance of T2WI–based was better.

Discussion

In the present study, we first proposed a nnU-Net–based deep learning network for the segmentation of basal cisterns in a multicenter dataset. The mean Dice coefficient in the testing dataset was 0.727, indicating that the segmentation model achieved acceptable results for the basal cistern segmentation. Then, we developed a radiomics signature based on the

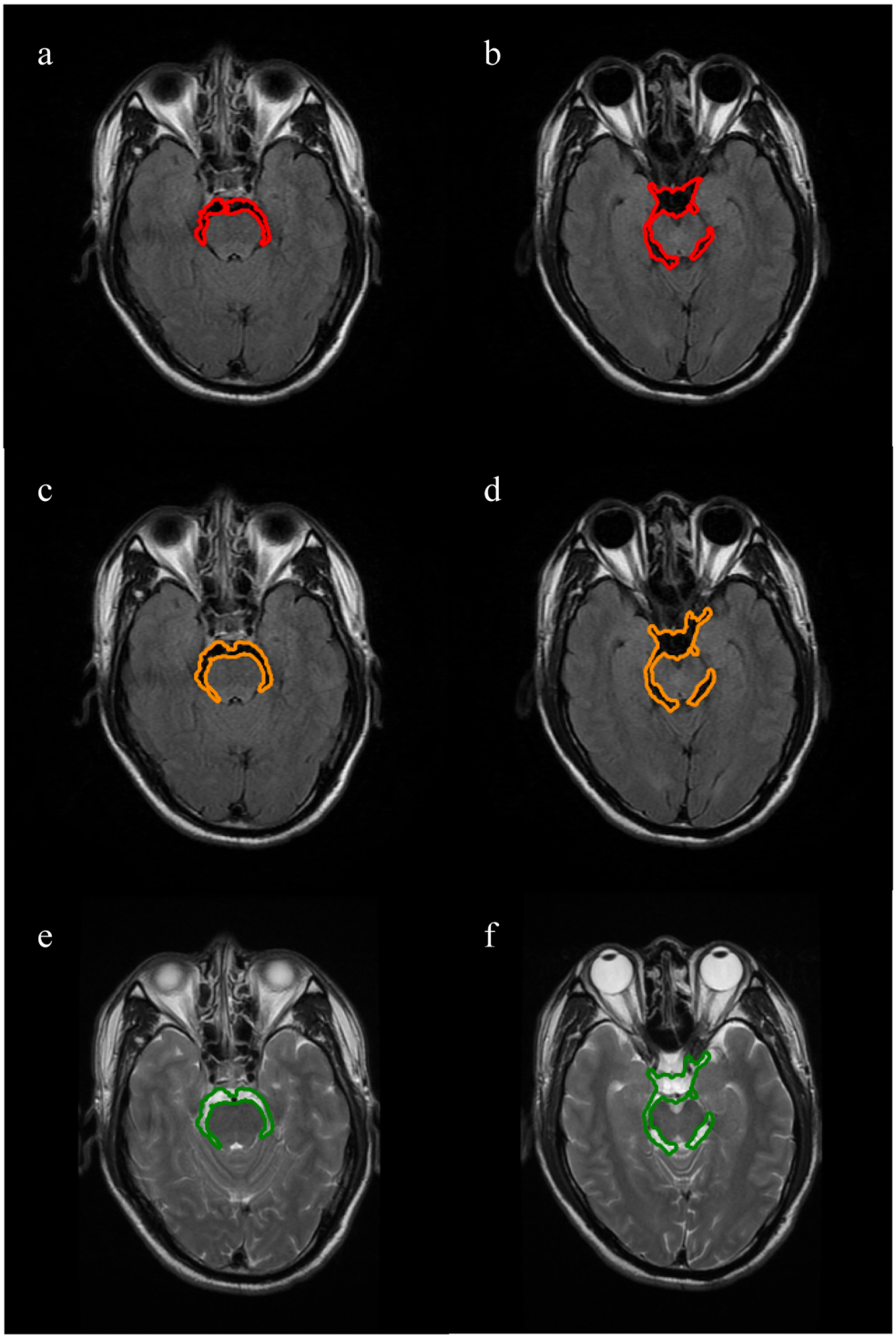

Fig. 3 Results of manual label and automatic segmentation of the basal cisterns. FLAIR images imposed with the manual label (**a**, **b**); FLAIR images imposed with automatic segmentation (**c**, **d**); T2W images imposed with automatic segmentation (**e**, **f**). FLAIR, fluid-attenuated inversion recovery; T2W, T2-weighted

segmentation of basal cisterns by nnU-Net using the same dataset. The T2WI–based radiomics signature developed using the SVM classifier showed a certain diagnostic significance for TBM, which might be unnoticeable by the naked eye on conventional MR images. Therefore, automatic segmentation of basal cisterns and the developed radiomics signature might provide supplemental data to assist in the diagnosis of TBM in a fully automatic manner, before the appearance of lesions with visible characteristics.

The pathology of TBM was found to be primarily caused by the host inflammatory response [26]. During the dissemination of *Mycobacteria* to the brain, some pro- and anti-inflammatory cytokines are induced [27]. Subsequently, granulomatous inflammation occurs in the subarachnoid space,

Table 3 Coefficients of features in the radiomics signatures

	Features	Coefficients
T2W	Original_firstorder_10Percentile	3.252
	Shape_MajorAxisLength	2.258
	Shape_SurfaceVolumeRatio	−1.941
	LoG-sigma-5-0-mm-3D_glszm_LowGrayLevelZoneEmphasis	−1.919
	LoG-sigma-5-0-mm-3D_firstorder_Skewness	1.904
	LoG-sigma-5-0-mm-3D_glcm_ClusterShade	0.748
	Shape_MinorAxisLength	0.302
FLAIR	Shape_SurfaceVolumeRatio	−0.957
	LoG-sigma-5-0-mm-3D_glrlm_GrayLevelNonUniformity	0.835
	Shape_MeshVolume	−0.747
	LoG-sigma-5-0-mm-3D_glszm_SizeZoneNonUniformityNormalized	0.589
	Original_glszm_SizeZoneNonUniformity	0.523
	LoG-sigma-5-0-mm-3D_gldm_SmallDependenceEmphasis	0.450
	Original_firstorder_TotalEnergy	0.416
	LoG-sigma-5-0-mm-3D_gldm_DependenceNonUniformity	0.383
	LoG-sigma-5-0-mm-3D_glszm_GrayLevelNonUniformity	−0.381
	Shape_MajorAxisLength	0.369
	LoG-sigma-5-0-mm-3D_glszm_SizeZoneNonUniformity	0.291
	LoG-sigma-5-0-mm-3D_firstorder_TotalEnergy	−0.263
	Shape_Maximum2DDiameterColumn	−0.037

FLAIR fluid-attenuated inversion recovery, *T2W* T2-weighted

mainly influencing the basal cisterns [28]. Besides, inflammatory exudates in basal cisterns can block the flow of cerebrospinal fluid (CSF), leading to hydrocephalus [28], and can also cause vasospasm and compression or strangulation of vessels [29]. Thus, basal meningeal enhancement is the primary radiologic feature of TBM, reflecting microabscess and intense inflammation of basal meninges. In our study, we used radiomics analysis to compare the deep image information of basal cisterns between the TBM and non-TBM groups. The results showed that there were certain differences between the two groups that could not be observed by the naked eye, which were significant to suggest the possibility of TBM.

To reduce the operator-dependent segmentation deviation and improve the work efficiency, an automatic segmentation model of basal cisterns was established using nnU-Net in the present study. It exhibited a high performance in the segmentation of basal cisterns in FLAIR images, as well as an acceptable capability to generalize by an external testing dataset. In addition, the automatic segmentation of basal cisterns should not be limited to the stage without lesions. The segmentation at different stages of TBM is also valuable for the assessment

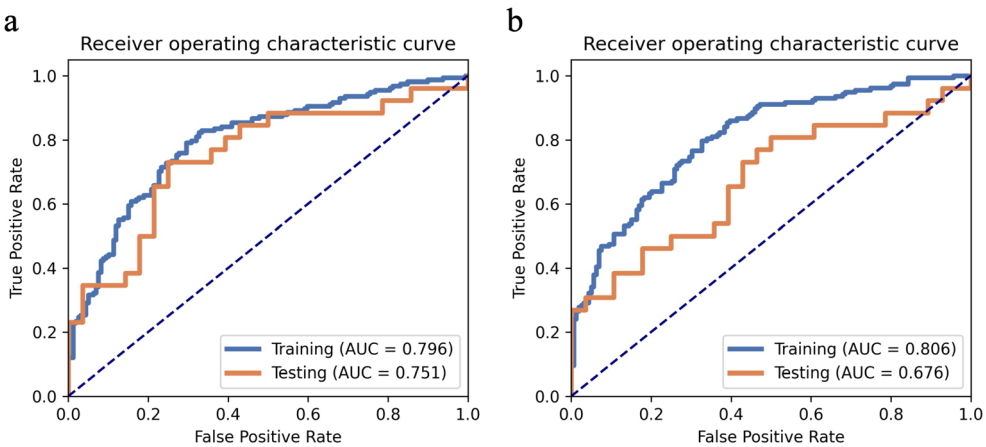

Fig. 4 ROC curves for T2WI–based radiomics signature (**a**) and FLAIR–based radiomics signature (**b**) in the training and testing datasets, respectively. In the testing dataset, the AUC of the T2WI–based radiomics signature reached 0.751, and the AUC of the FLAIR–based radiomics signature reached 0.676. AUC, area under the curve; FLAIR, fluid-attenuated inversion recovery; ROC, receiver operating characteristic; T2WI, T2–weighted imaging

Table 4 Performance of the radiomics signatures

	Metrics (95% CI)	T2WI–based	FLAIR–based
Training dataset	AUC	0.796 (0.744–0.847)	0.806 (0.759–0.853)
	Accuracy	0.748 (0.710–0.804)	0.735 (0.700–0.795)
	Sensitivity	0.829 (0.642–0.881)	0.797 (0.582–0.925)
	Specificity	0.667 (0.621–0.855)	0.673 (0.546–0.875)
Testing dataset	AUC	0.751 (0.617–0.886)	0.676 (0.529–0.823)
	Accuracy	0.741 (0.648–0.870)	0.648 (0.574–0.815)
	Sensitivity	0.731 (0.429–0.960)	0.808 (0.233–0.950)
	Specificity	0.750 (0.514–1.000)	0.500 (0.435–1.000)

AUC area under the curve, *CI* confidence interval, *FLAIR* fluid-attenuated inversion recovery, *T2W* T2-weighted

of response to therapy and disease prognosis. Further studies are therefore required to improve the quality of pixel-level segmentation and spatial-level detection.

The high-throughput extraction of large amounts of features from radiographic images possesses the advantages of objectivity, comprehensiveness, and repeatability, which may be significant for prediction of clinical results [10]. The selection of more features is associated with a higher dimensionality of input data, and the likelihood of overfitting consequently increases, resulting in a lower classification accuracy [30]. Our radiomics signature using the SVM classifier exhibited the best discrimination capability after

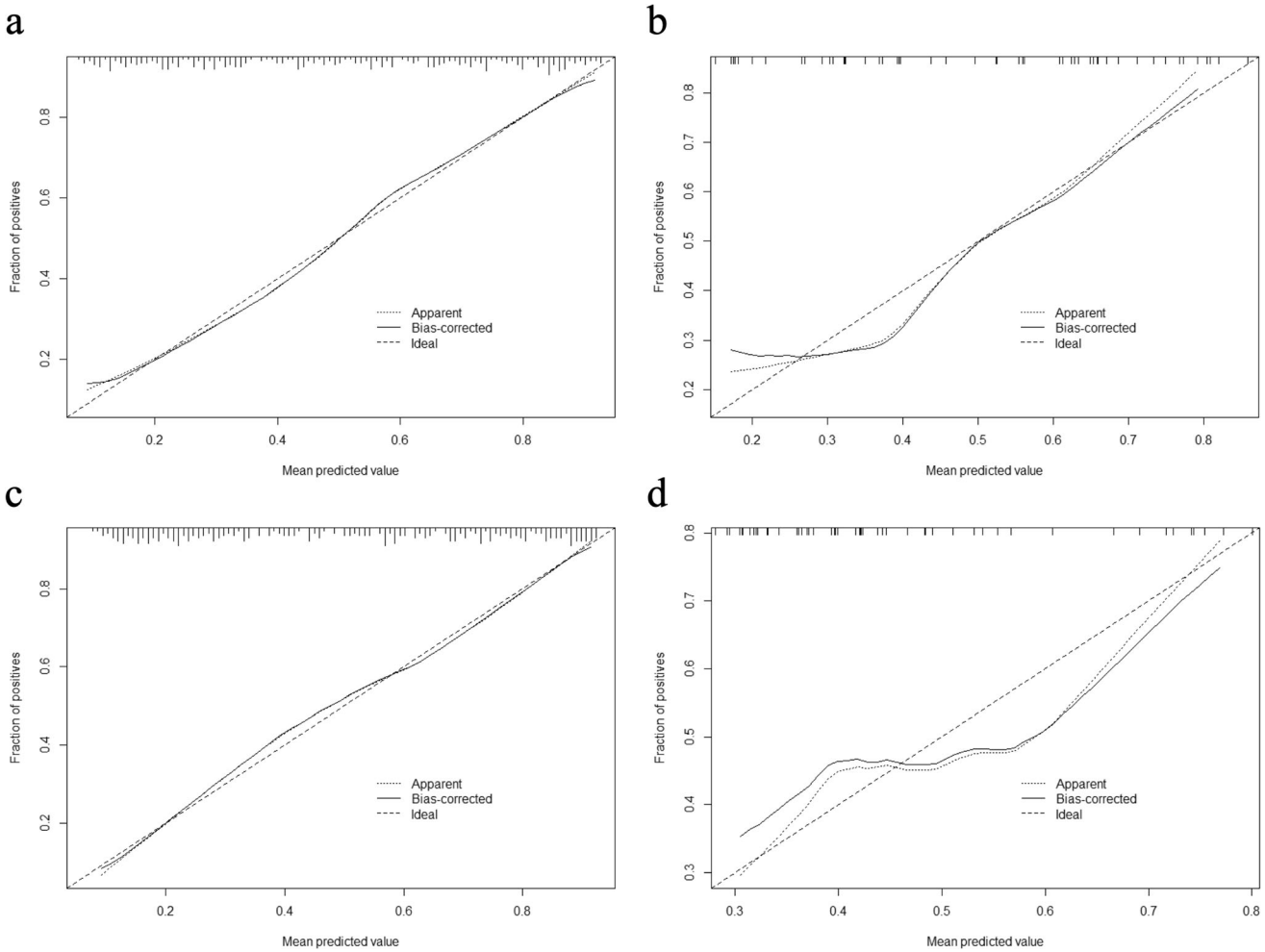

Fig. 5 Calibration curves for T2WI–based radiomics signature (**a**, **b**) and FLAIR–based radiomics signature (**c**, **d**) in the training and testing datasets, respectively. FLAIR, fluid-attenuated inversion recovery; T2WI, T2-weighted imaging

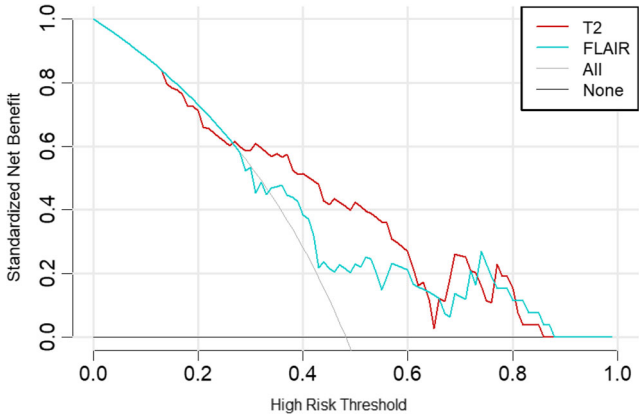

Fig. 6 Decision curve analysis for T2WI–based radiomics signature and FLAIR–based radiomics signature in the testing datasets. The *y*-axis represents the net benefit. The *x*-axis represents the threshold probability. The red line represents the net benefit of the T2WI–based radiomics signature. The blue line represents the net benefit of the FLAIR–based radiomics signature. FLAIR, fluid-attenuated inversion recovery; T2WI, T2-weighted imaging

selection of 7 T2WI features. Among these features, T2_shape_MajorAxisLength, T2_shape_SurfaceVolumeRatio, and T2_shape_MinorAxisLength were related to the shape and size of basal cisterns. Compared with the non-TBM group, the T2_shape_SurfaceVolumeRatio value was lower, and the values of the other two features were higher in the TBM group, which showed that the shape and size of basal cisterns were associated with the occurrence of intracranial TB infection. This might be related to the formation of thick exudates from basal cisterns in the early stage of TBM, which blocks subarachnoid and ventricular CSF pathways, resulting in communicating hydrocephalus [31]. T2_original_firstorder_10Percentile was the feature with the highest weight, and its value was higher in the TBM group, indicating hyperintense, which might be related to the accumulation of thick gelatinous exudates in basal cisterns [28]. T2_log-sigma-5-0-mm-3D_glszm_LowGrayLevelZoneEmphasis, a higher-order feature used to measure the distribution of lower gray-level size zones, further supported the significance of the above first-order features. Its negative higher value indicated that in the basal cisterns images of the non-TBM group, the proportion of lower gray-level values and size zones was greater. Notably, LoG filters were mainly used to suppress the image noise and to enhance the textural details, leading to the increased efficiency of capturing heterogeneity-associated features [32]. T2_log-sigma-5-0-mm-3D_firstorder_Skewness mainly represented the asymmetry of distribution. Similarly, the higher T2_log-sigma-5-0-mm-3D_glcm_ClusterShade value in the TBM group indicated that the GLCM lacked symmetry. Although these first-order or high-order features were difficult to identify by the human visual system, those all indicated the non-uniformity of the underlying tissue in the setting of basal cisterns from different dimensions.

In the current study, we attempted to perform manual and automatic segmentation of basal cisterns on FLAIR images. FLAIR sequences can better display lesions on the brain surface, the semi-oval area, and the brain tissue–CSF junction area by suppressing the signal intensity of CSF. In TBM, sulcal hyperintensity in basal cisterns can be observed on FLAIR images, which could be related to CSF protein concentration and effective echo time [33]. Therefore, FLAIR images assist clinicians to indicate whether there were lesions in the basal cisterns of TBM patients, and to reduce the interference of CSF and vascular signals during segmentation. However, the results showed that the radiomics signature developed based on T2W images had a greater diagnostic performance compared with the signature developed based on FLAIR images. This might be due to the circulatory disturbance of the CSF protein concentration in basal cisterns and the involvement of local cerebrovascular dysfunction during TBM; T2W images, which were sensitive to water in the tissue, were more suitable for radiomics feature extraction and signature construction.

There are some limitations to this study. First, this retrospective study involved only a single infectious agent, and its practical performance in the real clinical scenario needs to be verified by prospective study. In addition, the inclusion of other central nervous system infectious diseases for multi-classification research will help to improve the diagnostic system. Second, owing to the low sensitivity of etiological examination as the gold standard, we used a diagnostic scoring system to enroll TBM patients. Some subjective factors in the scoring system may also cause false-positive results. We could not completely eliminate the influence of such situation on the results. Finally, although we have used automatic segmentation based on nnU-Net to improve the reproducibility of the model, we should compare the influence of different harmonization schemes on the generalization of the model in large-scale multi-institutional studies.

In conclusion, our study proposed a fully automatic deep learning–based radiomics pipeline to identify invisible changes of basal cisterns in TBM. This strategy can warn radiologists about the elevated probability of occurrence of TBM and help improve its diagnosis.

Funding This work was supported by the Foundations of Shanghai Municipal Population and Family Planning Commission (201840146), and Science and Technology Commission of Shanghai Municipality (19411965800).

Declarations

Guarantor The scientific guarantor of this publication is Yuxin Shi.

Conflict of interest The authors of this manuscript declare no relationships with any companies, whose products or services may be related to the subject matter of the article.

Statistics and biometry No complex statistical methods were necessary for this paper.

Informed consent Written informed consent was waived by the Institutional Review Board.

Ethical approval Institutional Review Board approval was obtained.

Methodology
- retrospective
- diagnostic or prognostic study
- multicenter study

References

1. World Health Organization (2021) Global tuberculosis report 2021. World Health Organization, Geneva. Available via https://www.who.int/teams/global-tuberculosis-programme/tb-reports/global-tuberculosis-report-2021. Accessed 14 Oct 2021
2. Donovan J, Figaji A, Imran D, Phu NH, Rohlwink U, Thwaites GE (2019) The neurocritical care of tuberculous meningitis. Lancet Neurol 18:771–783
3. Imran D, Estiasari R, Maharani K et al (2018) Presentation, etiology, and outcome of brain infections in an Indonesian hospital: a cohort study. Neurol Clin Pract 8:379–388
4. Wang YY, Xie BD (2018) Progress on diagnosis of tuberculous meningitis. Methods Mol Biol 1754:375–386
5. Marais S, Thwaites G, Schoeman JF et al (2010) Tuberculous meningitis: a uniform case definition for use in clinical research. Lancet Infect Dis 10:803–812
6. Bernaerts A, Vanhoenacker FM, Parizel PM et al (2003) Tuberculosis of the central nervous system: overview of neuroradiological findings. Eur Radiol 13:1876–1890
7. Khatri GD, Krishnan V, Antil N, Saigal G (2018) Magnetic resonance imaging spectrum of intracranial tubercular lesions: one disease, many faces. Pol J Radiol 83:e524–e535
8. Wilkinson RJ, Rohlwink U, Misra UK et al (2017) Tuberculous meningitis. Nat Rev Neurol 13:581–598
9. Kumar S, Singh P, Vyas S et al (2021) Assessment of blood-brain barrier integrity in tuberculous meningitis using dynamic contrast-enhanced MR perfusion. Indian J Radiol Imaging 31:30–36
10. Lambin P, Rios-Velazquez E, Leijenaar R et al (2012) Radiomics: extracting more information from medical images using advanced feature analysis. Eur J Cancer 48:441–446
11. Reginelli A, Nardone V, Giacobbe G et al (2021) Radiomics as a new frontier of imaging for cancer prognosis: a narrative review. Diagnostics (Basel) 11:1796
12. Abdel Razek AAK, Alksas A, Shehata M et al (2021) Clinical applications of artificial intelligence and radiomics in neuro-oncology imaging. Insights Imaging 12:152
13. Stanzione A, Verde F, Romeo V, Boccadifuoco F, Mainenti PP, Maurea S (2021) Radiomics and machine learning applications in rectal cancer: current update and future perspectives. World J Gastroenterol 27:5306–5321
14. Kassner A, Liu F, Thornhill RE, Tomlinson G, Mikulis DJ (2009) Prediction of hemorrhagic transformation in acute ischemic stroke using texture analysis of postcontrast T1-weighted MR images. J Magn Reson Imaging 30:933–941
15. Arnold PG, Kaya E, Reisert M et al (2022) Support vector machine-based spontaneous intracranial hypotension detection on brain MRI. Clin Neuroradiol 32:225–230
16. Korez R, Likar B, Pernuš F, Vrtovec T (2016) Model-based segmentation of vertebral bodies from MR images with 3D CNNs. In: Ourselin S, Joskowicz L, Sabuncu MR, Unal G, Wells W (eds) Medical image computing and computer-assisted intervention – MICCAI 2016. Springer International Publishing, Cham, pp 433–441
17. Moeskops P, Wolterink JM, van der Velden BHM et al (2016) Deep learning for multi-task medical image segmentation in multiple modalities. In: Ourselin S, Joskowicz L, Sabuncu MR, Unal G, Wells W (eds) Medical Image Computing and Computer-Assisted Intervention – MICCAI 2016. Springer International Publishing, Cham, pp 478–486
18. Isensee F, Jaeger PF, Kohl SAA, Petersen J, Maier-Hein KH (2021) nnU-Net: a self-configuring method for deep learning-based biomedical image segmentation. Nat Methods 18:203–211
19. Savjani R (2021) nnU-Net: further automating biomedical image autosegmentation. Radiol Imaging. Cancer 3:e209039
20. Ma J, Wang Y, An X et al (2021) Toward data-efficient learning: a benchmark for COVID-19 CT lung and infection segmentation. Med Phys 48:1197–1210
21. Heller N, Isensee F, Maier-Hein KH et al (2021) The state of the art in kidney and kidney tumor segmentation in contrast-enhanced CT imaging: results of the KiTS19 challenge. Med Image Anal 67:101821
22. Huo L, Hu X, Xiao Q, Gu Y, Chu X, Jiang L (2021) Segmentation of whole breast and fibroglandular tissue using nnU-Net in dynamic contrast enhanced MR images. Magn Reson Imaging 82:31–41
23. Ronneberger O, Fischer P, Brox T (2015) U-Net: convolutional networks for biomedical image segmentation. In: Navab N, Hornegger J, Wells WM, Frangi AF (eds) Medical Image Computing and Computer-Assisted Intervention – MICCAI 2015. Springer International Publishing, Cham, pp 234–241
24. Song Y, Zhang J, Zhang YD et al (2020) FeAture Explorer (FAE): a tool for developing and comparing radiomics models. PLoS One 15:e0237587
25. van Griethuysen JJM, Fedorov A, Parmar C et al (2017) Computational radiomics system to decode the radiographic phenotype. Cancer Res 77:e104–e107
26. Davis AG, Rohlwink UK, Proust A, Figaji AA, Wilkinson RJ (2019) The pathogenesis of tuberculous meningitis. J Leukoc Biol 105:267–280
27. Simmons CP, Thwaites GE, Quyen NT et al (2006) Pretreatment intracerebral and peripheral blood immune responses in Vietnamese adults with tuberculous meningitis: diagnostic value and relationship to disease severity and outcome. J Immunol 176:2007–2014
28. Cresswell FV, Davis AG, Sharma K et al (2019) Recent developments in tuberculous meningitis pathogenesis and diagnostics. Wellcome Open Res 4:164
29. Choudhary N, Vyas S, Modi M et al (2021) MR vessel wall imaging in tubercular meningitis. Neuroradiology 63:1627–1634
30. Noble WS (2006) What is a support vector machine? Nat Biotechnol 24:1565–1567
31. Vadivelu S, Effendi S, Starke JR, Luerssen TG, Jea A (2013) A review of the neurological and neurosurgical implications of tuberculosis in children. Clin Pediatr (Phila) 52:1135–1143
32. Zhou X, Yi Y, Liu Z et al (2019) Radiomics-based pretherapeutic prediction of non-response to neoadjuvant therapy in locally advanced rectal cancer. Ann Surg Oncol 26:1676–1684
33. Kamran S, Bener AB, Alper D, Bakshi R (2004) Role of fluid-attenuated inversion recovery in the diagnosis of meningitis: comparison with contrast-enhanced magnetic resonance imaging. J Comput Assist Tomogr 28:68–72